Benchmark numerical solutions for two-dimensional fluid–structure interaction involving large displacements with the deforming-spatial-domain/stabilized space–time and immersed boundary–lattice Boltzmann methods

Yuan-Qing Xu[1], Yan-Qun Jiang[2], Jie Wu[3], Yi Sui[4,5] and Fang-Bao Tian[5]

Abstract

Body-fitted and Cartesian grid methods are two typical types of numerical approaches used for modelling fluid–structure interaction problems. Despite their extensive applications, there is a lack of comparing the performance of these two types of approaches. In order to do this, the present paper presents benchmark numerical solutions for two two-dimensional fluid–structure interaction problems: flow-induced vibration of a highly flexible plate in an axial flow and a pitching flexible plate. The solutions are obtained by using two partitioned fluid–structure interaction methods including the deforming-spatial-domain/stabilized space–time fluid–structure interaction solver and the immersed boundary–lattice Boltzmann method. The deforming-spatial-domain/stabilized space–time fluid–structure interaction solver employs the body-fitted-grid deforming-spatial-domain/stabilized space–time method for the fluid motions and the finite-difference method for the structure vibrations. A new mesh update strategy is developed to prevent severe mesh distortion in cases where the boundary does not oscillate periodically or needs a long time to establish a periodic motion. The immersed boundary–lattice Boltzmann method uses lattice Boltzmann method as fluid solver and the same finite-difference method as structure solver. In addition, immersed boundary method is used in the immersed boundary–lattice Boltzmann solver to handle the fluid–structure interaction coupling. Results for the characteristic force coefficients, tail position, plate deformation pattern and the vorticity fields are presented and discussed. The present results will be useful for evaluating the performance and accuracy of existing and new numerical methodologies for fluid–structure interaction.

Introduction

Fluid–structure interaction (FSI) phenomena are ubiquitous in our daily life. Study of FSI is of great significance to understand many important biological phenomena and improve engineering designs that involve flexible components. Some representative examples include the flag flapping that can provide inspiration to designing the flexible plate energy harvester by using piezoelectric materials,[1–7] the flexible flapping wing that can provide better aerodynamic performance,[8–10] and the vocal fold vibration that is important to understand phonation.[11–13] Due to their

[1]School of Life Science, Beijing Institute of Technology, Beijing, China
[2]Department of Mathematics, Southwest University of Science and Technology, Mianyang, Sichuan, China
[3]Department of Aerodynamics, Nanjing University of Aeronautics and Astronautics, Nanjing, Jiangsu, China
[4]School of Engineering and Materials Science, Queen Mary University of London, London, UK
[5]School of Engineering and Information Technology, University of New South Wales, Canberra, Australia

Corresponding author:
Fang-Bao Tian, School of Engineering and Information Technology, University of New South Wales, Canberra ACT 2600, Australia.
Email: f.tian@adfa.edu.au

fundamental importance and practical engineering applications, great efforts have been made to study FSI problems.[14–16]

During the past two decades, various numerical methods have been developed for solving FSI problems, some of which were summarized by Deng et al.[14] Based on the mesh used, these methods can be classified into two typical types of approaches: body-fitted grid methods and Cartesian grid methods.

The body-fitted grid methods employ a mesh that is generated to fit the boundaries immersed in the fluid. In the problems with moving boundaries, the mesh needs to be adjusted according to the boundary motion at each time step so that the mesh boundary conformality is reserved. The mesh could be severely distorted for large-deformed-boundary problems, and consequently may need to be regenerated. The major advantage of body-fitted grid methods is associated with the fact that the boundary conditions (usually the Dirichlet type velocity boundary conditions) can be directly applied at the moving boundaries. Therefore, they generally have higher-order accuracy on the nodes near or at the boundaries. The DSD/SST method (see literature[2,17–23] for the method details and its improved versions, and see literature[3,15,16,24–30] for application examples) is a representative body-fitted grid method for complex fluid dynamics and FSI simulations. In this method, the stabilization strategies, streamline-upwind/Petrov–Galerkin[31,32] and pressure-stabilizing/Petrov–Galerkin,[17,33] are used to enhance numerical stability. More importantly, this method allows the computational mesh or the overall computational domain at various time levels to vary without introducing additional interpolation schemes if the computational domain topology is preserved. Therefore, it can be effectively applied to simulate complex flows and FSI problems where moving boundaries and interfaces are involved.[17–19] Since its birth, the DSD/SST method has been extensively used to model complex flows and FSI, such as animal swimming and flight,[29,30,34–45] flag flapping,[2,3] and non-Newtonian flow.[28,46] Body-fitted grid methods could be time consuming and complicated due to the difficulties associated with grid generation in complex geometries and mesh movement/re-generation in large displacement/deformation problems.

In Cartesian grid methods, the fluid governing equations are discretized on a Cartesian mesh which does not conform to the immersed boundaries which significantly simplifies grid generation and avoids mesh movement/regenration. The immersed boundary method (IB method)[47–49] is a popular approach based on Cartesian grid. In the IB method, the boundary conditions at the immersed boundaries are achieved by spreading the stresses exerted by the boundaries on the fluid onto the fluid nodes near the boundaries. Recently, the LB method has attracted growing interest on expanding its applications and proposing new features to improve its performance.

For example, to reduce the computational cost, multi-block technique, adaptive grid, and curvilinear mesh have been applied.[50–52] To combine the advantages of IB method and the simple formulation and high level of scalability on parallel processing systems of the LB method, IB-LB method has been developed for complex geometries and complex flows.[4,53–57] In order to improve the numerical stability in the FSI problems involving heavy structures, an inertia penalty idea, originally presented in Kim and Peskin,[58] has been extended into the IB-LB method.[4,5,7,56,59] In our recent work,[13] an IB fluid solver and a nonlinear finite-element structure solver are coupled to assemble an FSI method for large-deformation FSI problems. In this solver, three relaxation parameters were proposed to relax the quantities at the FSI interface including the forces, displacement and velocity. Later, this FSI coupling strategy has been further improved and applied to a variety of biological problems.[8,11–13,29,30,60,61] Though IB method has many advantages in handling computational mesh, it is hard to control the mesh size within the boundary layer.[49]

Although both body-fitted and Cartesian grid methods have been extensively applied to FSI problems, seldom effort has been made to compare their performance. This is the motivation of the present work. Here we consider two typical FSI problems: flow-induced vibration of a highly flexible plate in an axial flow and a pitching flexible plate.[1–7,13,29,30] Previous effort has been made to study the vibration patterns of a highly flexible plate in an axial flow, and both deformation and total force of a pitching flexible plate. For future validation purpose, more data are required, including deformation, vibration patterns, pressure drag, viscous drag and local force distribution. In this work, we will provide these data focusing on the cases of large displacements simulated by partitioned FSI methods: the DSD/SST FSI solver comprising of the DSD/SST fluid solver and the finite-difference (FD) structure solver[29,30] with an updated mesh moving strategy, and the IB–LB FSI solver based on the LB method for the fluid dynamics, the same FD method for the structural dynamics and IB method for FSI coupling.

This paper is organized as follows. The fluid and structure governing equations are introduced in the Governing equations section. The Numerical methods section briefly introduces the numerical approaches. Results for two cases, flow-induced vibration of a highly flexible plate in an axial flow and a pitching flexible plate, are presented in the Results and discussion section. Final conclusions are given in the Conclusion section.

Governing equations

In this paper, the two-dimensional FSI problems involving incompressible, viscous fluid flow and non-linear structures are considered. Assume that the

computational domain is Ω_t and the temporal region we are interested in is $(0, T_0)$. The non-dimensional Navier–Stokes equations for the fluid flow are given as follows

$$\frac{\partial \boldsymbol{u}}{\partial t} + \boldsymbol{u} \cdot \nabla \boldsymbol{u} - \nabla \cdot \sigma = 0, \quad \nabla \cdot \boldsymbol{u} = 0,$$
$$\text{on } \Omega_t \times (0, \ T_0) \tag{1}$$

where $\boldsymbol{u}$ is the velocity and σ is the stress tensor. For Newtonian fluid, the stress tensor is determined by

$$\sigma_{ij} = -p\delta_{ij} + \left(\frac{\partial u_i}{\partial x_j} + \frac{\partial u_j}{\partial x_i}\right)\Big/\mathrm{Re} \tag{2}$$

where p is the fluid pressure, and Re is the Reynolds number. In this work, Re is defined as $\mathrm{Re} = \rho U L / \mu$, where ρ and μ are respectively the fluid density and viscosity, L is the characteristic length (i.e. the length of the flexible plate), and U is the characteristic velocity (i.e. the incoming flow velocity). Note that in equation (1), U, L, $L \ / \ U$ and ρU^2 have been used to re-scale the velocity $\boldsymbol{u}$, coordinate $\boldsymbol{x}$, time t and pressure p, respectively.

The boundary conditions for fluid (Γ) can be divided into the Dirichlet type (Γ_g) and the Neumann type (Γ_h), which are given as follow

$$\boldsymbol{u} = \boldsymbol{u}_g, \quad \text{on } \Gamma_g, \quad \boldsymbol{n} \cdot \sigma = \boldsymbol{h}_g, \quad \text{on } \Gamma_h \tag{3}$$

where Γ_g comprises of the inflow boundary and FSI interface, and Γ_h includes the outflow boundary.

The governing equation for structure dynamics is given as[4,29,30]

$$S\frac{\partial^2 \boldsymbol{X}}{\partial t^2} - \frac{\partial}{\partial s}\left[K_S\left(|\frac{\partial \boldsymbol{X}}{\partial s}| - 1\right)\frac{\partial \boldsymbol{X}}{\partial s}\right] + K_B\frac{\partial^4 \boldsymbol{X}}{\partial s^4} = \boldsymbol{F},$$
$$\text{on } [0, L] \times (0, T_0) \tag{4}$$

where $\boldsymbol{X}$ is the Lagrangian coordinate of the plate, s is the arc length starting from the leading edge, $\boldsymbol{F}$ is the hydrodynamic traction, S is the mass ratio, $T(s) = K_S(|\frac{\partial \boldsymbol{X}}{\partial s}| - 1)$ is the tension force within the plate, and K_B and K_S are, respectively, the non-dimensional bending and stretching coefficients. The non-dimensional parameters are defined as $S = m_s/(\rho L)$, $K_B = E_B/(\rho U^2 L^3)$, and $K_S = E_S/(\rho U^2 L)$ where m_s is the linear density, and E_B and E_S are the bending and stretching coefficient, respectively.

In order to directly compare the results predicted by the body-conformal mesh method and the Cartesian mesh method, two problems are conducted: flow-induced vibration of a highly flexible plate in an axial flow and a pitching flexible plate. Three types of boundary conditions are encountered here.

For the flow-induced vibration of a highly flexible plate in an axial flow, the simply supported boundary condition is applied at the leading edge, i.e.

$$\boldsymbol{X} = \boldsymbol{X}_0(t), \quad \frac{\partial^2 \boldsymbol{X}}{\partial s^2} = 0 \tag{5}$$

At the trailing edge, the free end boundary condition (i.e., zero moment and zero transverse stress) is applied[62]

$$\frac{\partial^2 \boldsymbol{X}}{\partial s^2} = 0, \quad \frac{\partial^3 \boldsymbol{X}}{\partial s^3} = 0 \tag{6}$$

For the flow over a pitching flexible plate, the leading edge motions including the position and orientation are prescribed as

$$\boldsymbol{X} = \boldsymbol{X}_0(t), \quad \frac{\partial \boldsymbol{X}}{\partial s} = [\cos(\beta(t)), \sin(\beta(t))] \tag{7}$$

Similarly, the boundary condition described by equation (6) is applied at the free end.

Numerical methods

The numerical methods used in this work are two partitioned FSI methods given in our previous work.[4,29,30] The first one is the DSD/SST FSI method which combines the DSD/SST fluid solver and the FD structure solver. The only difference is that we modify the mesh moving strategy to prevent severe mesh distortion in cases where the boundary does not oscillate periodically or needs a long time to establish a periodic motion. The other one is the IB–LB method using LB method for the fluid dynamics, the FD method for the structure dynamics and IB method for the FSI coupling.

DSD/SST FSI method

The DSD/SST FSI method used here was presented in literature[29,30] and is introduced below briefly for completeness. The reader is referred to the references provided for more details of this solver and its applications. This solver employs the DSD/SST method, first given by Tezduyar,[20] for fluid dynamics. The time-changing fluid domain ($\Omega_t \times (0, T_0)$) is divided into a series of space–time slabs Q_n which is enclosed by Ω_n, Ω_{n+1} and P_n, where Ω_n and Ω_{n+1} are, respectively, computational domain at t_n and t_{n+1}, and P_n is the lateral surface of Q_n described by the boundary Γ as t traverses from t_n to t_{n+1}. Now, we can describe the DSD/SST formulation as follows: Given $(\boldsymbol{u}^h)_n^-$ (i.e. the flow field at Ω_n in Q_{n-1}), find $\boldsymbol{u}^h \in \left(S_u^h\right)_n$ and $p^h \in \left(S_p^h\right)_n$ such that $\forall \boldsymbol{w}^h \in \left(V_u^h\right)_n$ and

$\forall q^h \in \left(V_p^h\right)_n$, the following variational formulation is satisfied

$$
\int_{Q_n} w^h \cdot \left(\frac{du^h}{dt}\right) dQ + \int_{Q_n} \epsilon(w^h) : \sigma^h dQ
$$
$$
- \int_{(P_n)_h} w^h \cdot h \, dP + \int_{Q_n} q^h \nabla \cdot u^h dQ
$$
$$
+ \sum_{e=1}^{nel} \int_{Q_n^e} \tau \left(\frac{du^h}{dt} + \nabla p^h - \frac{2}{Re}\nabla \cdot (\epsilon(u^h))\right)
$$
$$
\cdot \left(\frac{dw^h}{dt} + \nabla q^h\right) dQ + \sum_{e=1}^{nel} \int_{Q_n^e} \delta(\nabla \cdot w^h)(\nabla \cdot u^h) dQ
$$
$$
+ \int_{\Omega_n} (w_n^h)^+ \cdot \left((u^h)_n^+ - (u^h)_n^-\right) d\Omega = 0
\tag{8}
$$

where the following notation are used

$$
\frac{d(\cdots)^h}{dt} = \frac{\partial(\cdots)^h}{\partial t} + u^h \cdot \nabla(\cdots)^h
\tag{9}
$$

$$
\int_{Q_n} (\cdots) dQ = \int_{I_n} \int_{\Omega_t^h} (\cdots) d\Omega \, dt
\tag{10}
$$

$$
\int_{P_n} (\cdots) dP = \int_{I_n} \int_{\Gamma_t^h} (\cdots) d\Gamma \, dt
\tag{11}
$$

$$
(u_h)_n^\pm = \lim_{\varepsilon \to 0} u(t_n \pm \varepsilon)
\tag{12}
$$

$$
\epsilon(A) = \frac{1}{2}(\nabla A + \nabla A^T)
\tag{13}
$$

In equation (8), τ and δ are the stabilization parameters determined by

$$
\tau = \frac{h}{2\sqrt{u^2 + v^2}}\zeta(Re^h), \quad \delta = \frac{h\sqrt{u^2 + v^2}}{2}\zeta(Re^h)
\tag{14}
$$

where h is the mesh size, and $\zeta(z)$ and Re^h are given by

$$
\zeta(z) = \begin{cases} z, z \leqslant 1, \\ 1, z > 1, \end{cases} \quad Re^h = \frac{h\sqrt{u^2 + v^2}Re}{12}
\tag{15}
$$

Here the equal-order basis functions are employed for both velocity and pressure as those used in the original DSD/SST method.[33] The Gaussian quadrature is used to achieve numerical integration over the element.[63] The non-linear terms are handled by the Newton–Raphson method.[64,65] Finally the linear system of algebraic equations resulting from the space–time finite-element discretization is solved by GMRES (generalized minimal residual) method.[66,67] The spatial discretization of structure governing equation is handled by the second-order FD method,

and the temporal discretization is achieved by[68]

$$
S(2X^{n+1} - 5X^n + 4X^{n-1} - X^{n-2})/\Delta t^2 = \mathbf{RHS}^{n+1}
\tag{16}
$$

where $\mathbf{RHS}$ includes all terms excluding inertial term. Its discretized form can be written as

$$
\mathbf{RHS}_l = F_l + D_s(K_S(|D_s X_l| - 1)t)
$$
$$
- K_B \sum_{m=2}^{n_f - 1} (X_{m+1} - 2X_m + X_{m-1})
$$
$$
(-\delta_{m+1,l} + 2\delta_{m,l} - \delta_{m-1,l})/\Delta s^4
$$

where n_f is the total number of nodes on the plate, Δs is the Lagrangian grid spacing, D_s is the second-order central difference operator with respect to s, and t is the tangential vector. When $l = 1$ and n_f, boundary conditions are considered for evaluating D_s.

The fluid dynamics, i.e. equation (1), and the structural dynamics, i.e. equation (4), are coupled through the boundary conditions, i.e.

$$
u = u_b, F = [\sigma_+ - \sigma_-] \cdot n
\tag{17}
$$

where u_b is the structure velocity obtained from the structural solver. "$-$", "$+$" and the normal vector n are defined in Figure 1. In the numerical applications, $\sigma_\pm \cdot n$ is determined by[69,70]

$$
\sigma_\pm \cdot n = -p_\pm n + (w_\pm \times n)/Re
\tag{18}
$$

where $w = \nabla \times u$ is the vorticity. The discretized equations of fluid and structural dynamics are solved by using a partitioned coupling (also known as the block-iterative coupling) method. The details of this method, as well as the stability strategy and applications can be found in literature.[6,8,12,13,29, 30,60]

To achieve the mesh movement, the fluid computational domain is treated as a linear elastic body, and the displacement of the moving mesh $d^*(x, y)$ is governed by

$$
\nabla \cdot \sigma^* = 0, \quad \{\sigma^*\} = \{D\}\{\varepsilon^*\}
\tag{19}
$$

where $\{\sigma^*\} = (\sigma_x^*, \sigma_y^*, \sigma_{xy}^*)^T$ is the elastic stress, $\{\varepsilon^*\} = (\varepsilon_x^*, \varepsilon_y^*, \varepsilon_{xy}^*)^T = (\partial d_x^*/\partial x, \partial d_y^*/\partial y, \partial d_x^*/\partial y + \partial d_y^*/\partial x)^T$ is the strain, and $\{D\}$ is stiffness matrix written as

$$
\{D\} = \frac{E_m}{1 - v_m^2}\begin{pmatrix} 1 & v_m & 0 \\ v_m & 1 & 0 \\ 0 & 0 & 0.5(1 - v_m) \end{pmatrix}
$$

where E_m is the elastic modulus and v_m is the Poisson's ratio. The far field boundaries are fixed. The displacements of internal boundaries between consecutive time steps are applied at the moving boundaries. This linearized system is solved by using

the GMRES method.[66,67] Here d^* can be taken as an increment of mesh between two time steps. If it is taken as the increment of between two consecutive time steps, the mesh movement is achieved by $x^{n+1} = x^n + d^{*n}$. In practical applications, the stiffness coefficient is a function of the distance to the inner/moving boundaries: it is larger near the inner/moving boundaries where the elements are small and vice versa.[71,72]

For problems involving periodic oscillatory boundaries (e.g. prescribed flapping foil), the grids at each step in the first cycle can be saved and reused in the remaining cycles. Such treatment could save the computational expense and maintain the mesh quality. In many FSI computations, the boundary does not oscillate periodically or needs a long time to establish a periodic motion. In this situation, the distortion of elements might be severe, which significantly affects the accuracy of the results. To avoid the severe mesh distortion, traditional treatment is to regenerate the mesh. Here we prevent mesh distortion by using the following method. If the mesh quality is good, we update mesh x_{np}^{n+1} based on x_{np}^n, as discussed above. If the mesh quality is bad, the mesh x_{np}^{n+1} is achieved with a "restart method" which is based on the initial mesh by using increment method. It is computationally expensive if the mesh quality is checked at each time step. Therefore, we directly prescribe that the normal mesh update is used from $kM + 1$ to $(k + 1)M - 1$ steps, and the restart method is used at $(k + 1)M$ step where k is a natural number. Such treatment requires no mesh regeneration without significant increase of computational expense. In the current applications, $M = 1000$, and five increment sub-steps are used. The computational time increase for mesh update is about 4‰ which is true for three-
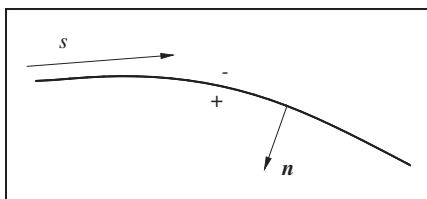

Figure 1. A segment of a flexible plate.

dimensional simulations and ignorable compared to the fluid solver. Figure 2 shows the mesh around a pitching plate of $K_B = 0.0625$ at $t/T = 6.0$ where the fluid computational domain is a rectangular box spanning over $(-2L, -3L) \times (14L, 3L)$ and the plate is located at origin point. It is clearly shown that the mesh quality by the present mesh moving strategy is significantly improved. It is also found that a larger computational domain could improve the mesh quality. However, it requires more elements and thus needs more computational time.

The validation and verification of the DSD/SST method for fluid dynamics can be found in the references as discussed in the introduction. The DSD/SST solver used in this work has been validated and applied to many problems including stationary, prescribed moving and FSI boundaries.[14,28,29,36,41,44,45,73] The structure solver was validated in Tian,[29] and the FSI solver was presented in literature.[29,30]

IB–LB FSI method

In the IB-LB FSI solver, the LB method is employed to acquire the fluid dynamics. Here single relaxation time discrete lattice Boltzmann equation is used[4,74–76]

$$
\begin{aligned}
&g_i(\mathbf{x} + \mathbf{e}_i\Delta t, t + \Delta t) - g_i(\mathbf{x}, t) \\
&= -\frac{1}{\tau}[g_i(\mathbf{x}, t) - g_i^{eq}(\mathbf{x}, t)] + \Delta t G_i
\end{aligned}
\tag{20}
$$

where $g_i(\mathbf{x}, t)$ is the distribution function for particles, $\mathbf{e}_i$ is the particle velocity, $\mathbf{x}$ is the particle position, Δt is the time step size, $g_i^{eq}(\mathbf{x}, t)$ is the equilibrium distribution function, τ is the relaxation time, and G_i considers fluid body force effect. In equation (20), g_i^{eq} and G_i are determined by

$$
g_i^{eq} = \omega_i \rho \left[1 + \frac{\mathbf{e}_i \cdot \mathbf{u}}{c_s^2} + \frac{\mathbf{u}\mathbf{u} : (\mathbf{e}_i\mathbf{e}_i - c_s^2\mathbf{I})}{2c_s^4} \right]
\tag{21}
$$

$$
G_i = \left(1 - \frac{1}{2\tau} \right)\omega_i \left[\mathbf{e}_i - \mathbf{u} + \frac{\mathbf{e}_i \cdot \mathbf{u}}{c_s^2}\mathbf{e}_i \right] \cdot \frac{\mathbf{f}}{c_s^2}
\tag{22}
$$

where ω_i is the weighing factor, $\mathbf{u}$ is the fluid velocity, c_s is the lattice sound speed defined by $c_s = \Delta x/\sqrt{3}\Delta t$, and $\mathbf{f}$ is the body force due to the immersed
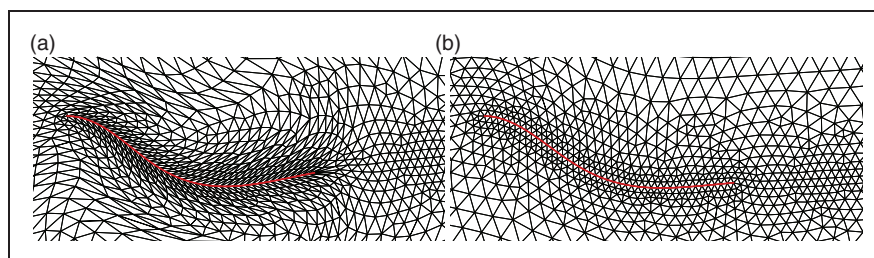

Figure 2. Mesh around a pitching plate of $K_B = 0.0625$ at $t/T = 6.0$. (a) Original mesh moving strategy; (b) New mesh moving strategy in this work.

boundaries. The connection between the relaxation time and the fluid kinematic viscosity in the Navier–Stokes equations is

$$\nu = (\tau - 0.5)c_s^2 \Delta t \tag{23}$$

In this work, the D2Q9 (two-dimensional nine-speed) model[77] is used. In this model, the particle velocities are given as

$$\mathbf{e}_0 = (0, 0)$$
$$\mathbf{e}_i = \left(\cos\frac{\pi(i-1)}{2}, \ \sin\frac{\pi(i-1)}{2} \right) \frac{\Delta x}{\Delta t}$$
$$\text{for } i = 1 \text{ to } 4$$
$$\mathbf{e}_i = \left(\cos\frac{\pi(i-9/2)}{2}, \ \sin\frac{\pi(i-9/2)}{2} \right) \frac{\sqrt{2}\Delta x}{\Delta t}$$
$$\text{for } i = 5 \text{ to } 8$$

where Δx is the lattice spacing. The values of $\mathbf{e}_i$ above ensure that within one time step, a LB particle moves to one of the eight neighboring nodes or stays at its current location. In the model used here, ω_i are given by $\omega_0 = 4/9$, $\omega_i = 1/9$ for $i = 1$ to 4 and $\omega_i = 1/36$ for $i = 5$ to 8.

Once the particle density distribution is known, the fluid macro quantities (i.e. density, velocity and pressure) are obtained from

$$\rho = \sum_i g_i \tag{24}$$

$$\mathbf{u} = \frac{\sum_i \mathbf{e}_i g_i + \frac{1}{2}\mathbf{f}\Delta t}{\rho} \tag{25}$$

$$p = \rho c_s^2 \tag{26}$$

Please note that the single-relaxation-time LB model is used in this work. For the parameter considered in this work, this model does not introduce any undesirable errors as reported in work by Chai.[78]

In the IB method used here, a smooth body force is distributed to the Cartesian grids in the vicinity of the immersed boundaries in order to achieve the boundaries conditions (as described in equation (17)),

$$\mathbf{f} = \int \mathbf{F}(s, t)\delta_D(\mathbf{x} - \mathbf{X}(s, t))\mathrm{d}s \tag{27}$$

where $\delta_D(\mathbf{x} - \mathbf{X}(s, t))$ is the Dirac's delta function, and $\mathbf{F}(s, t)$ is the Lagrangian force density determined by $\mathbf{F} = \alpha_1(\mathbf{X} - \mathbf{x}_{ib}) + \alpha_2(\mathbf{U} - \mathbf{u}_{ib})$. Here $\mathbf{U}$ is the boundary velocity, $\mathbf{u}_{ib}$ is the interpolated velocity using flow field, $\mathbf{X}$ is the boundary position, $\mathbf{x}_{ib}$ is the position integrated by using $\mathbf{u}_{ib}$, and α_1 and α_2 are positive constants.

Our IB–LB FSI solver has been validated and applied to several problems including flow-induced flapping of flexible plate(s) and cell(s)/capsule(s).[4,5,7,56,59,79–81] Other applications of the IB–LB method can be found in literature.[53,55,82–85]

Forces and coefficients

To quantitatively discuss the behaviors of the flexible plate, some characteristic parameters including stress, forces and coefficients are defined here. In the DSD/SST method, the stress on the up ("+") and bottom ("−") sides of the plate is calculated by

$$\boldsymbol{f}_\pm = \pm\boldsymbol{\sigma}_\pm \cdot \boldsymbol{n} = \mp p_\pm \boldsymbol{n} \pm (\boldsymbol{w}_\pm \times \boldsymbol{n})/\mathrm{Re} \tag{28}$$

which can be divided into the viscous stress $\boldsymbol{f}_f$ and the pressure stress $\boldsymbol{f}_p$. The total forces (F_x and F_y) are then acquired by

$$F_x = \int_L (f_{x,+} + f_{x,-})\mathrm{d}s \tag{29}$$

$$F_y = \int_L (f_{y,+} + f_{y,-})\mathrm{d}s \tag{30}$$

Finally, the drag and the lift coefficients can be written as

$$C_D = F_x/(0.5\rho U^2 L) \tag{31}$$

$$C_L = F_y/(0.5\rho U^2 L) \tag{32}$$

where C_D can be further divided into the viscous drag coefficient $C_{D,f}$ and the pressure drag coefficient $C_{D,p}$. In the IB–LB FSI method, the drag and lift forces are obtained by integrating the Lagrangian forces along the plate. This treatment does not increase complicity compared to the momentum-exchange method.[86]

Results and discussion

Flow-induced vibration of a highly flexible plate in an axial flow

We first consider a highly flexible plate of length L that is fixed in an axial flow, as shown in Figure 3. The fluid computational domain is a rectangular box, i.e. $(-2L, -3L) \times (14L, 3L)$. In the DSD/SST solver, the element number is around 1.5×10^4 and the time step is $0.0033333L/U$ which leads to about 800–900 time steps during a flapping cycle. In the IB–LB solver, the computational domain is discretized by 800×300 Cartesian nodes (i.e. $\Delta x = \Delta y = 0.02L$), and $dt = 0.001L/U$. Simulations are carried out to ensure that the results are independent on the mesh size and time step. Two cases are performed: $K_B = 10^{-4}$ and 10^{-3}. In the computations, other parameters are $\beta = 0°$, $\mathrm{Re} = 100$, $S = 1$, and $K_S = 500$.
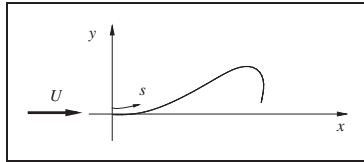
Figure 3. Schematic of a highly flexible plate (filament) in an axial flow.

Table 1. Flow-induced vibration of a highly flexible plate in an axial flow: amplitude of the Y-displacement of the free point, the Strouhal number St = L/(UT), and the average drag coefficient.

Cases	Sources	A_m/L	St	$\overline{C_D}$
$K_B = 10^{-4}$	DSD/SST	0.912	0.322	0.941
	IB–LB	0.904	0.309	0.948
$K_B = 10^{-3}$	DSD/SST	0.926	0.306	0.856
	IB–LB	0.886	0.299	0.878

Simulations are conducted until the vibration of the plate is periodic. In Table 1, we present vibration amplitude, St = L/(UT) (T is the flapping period) and average drag coefficient. Figures 4 to 7 show the force coefficients, tail position, deformation pattern of the plate, and vorticity fields.

The results show that both the DSD/SST method and the IB–LB method are able to capture the major flow features, though some discrepancies are observed during fast transient periods. Specifically, the difference of amplitude is 1% for $K_B = 10^{-4}$ and 4% for $K_B = 10^{-3}$; the difference of frequency is 4% for $K_B = 10^{-4}$ and 2% for $K_B = 10^{-3}$; and the difference of average drag is 1% for $K_B = 10^{-4}$ and 3% for $K_B = 10^{-3}$ (see Table 1). The asymmetric behavior when the plate moves from 1 to 2, and from 2 to 3 (as marked in Figure 4(g) and (h)), is captured by both methods. This is a phenomenon analog to the crack of the whip, which was discussed for flags in Connell and Yue[68] as a snapping event. When we
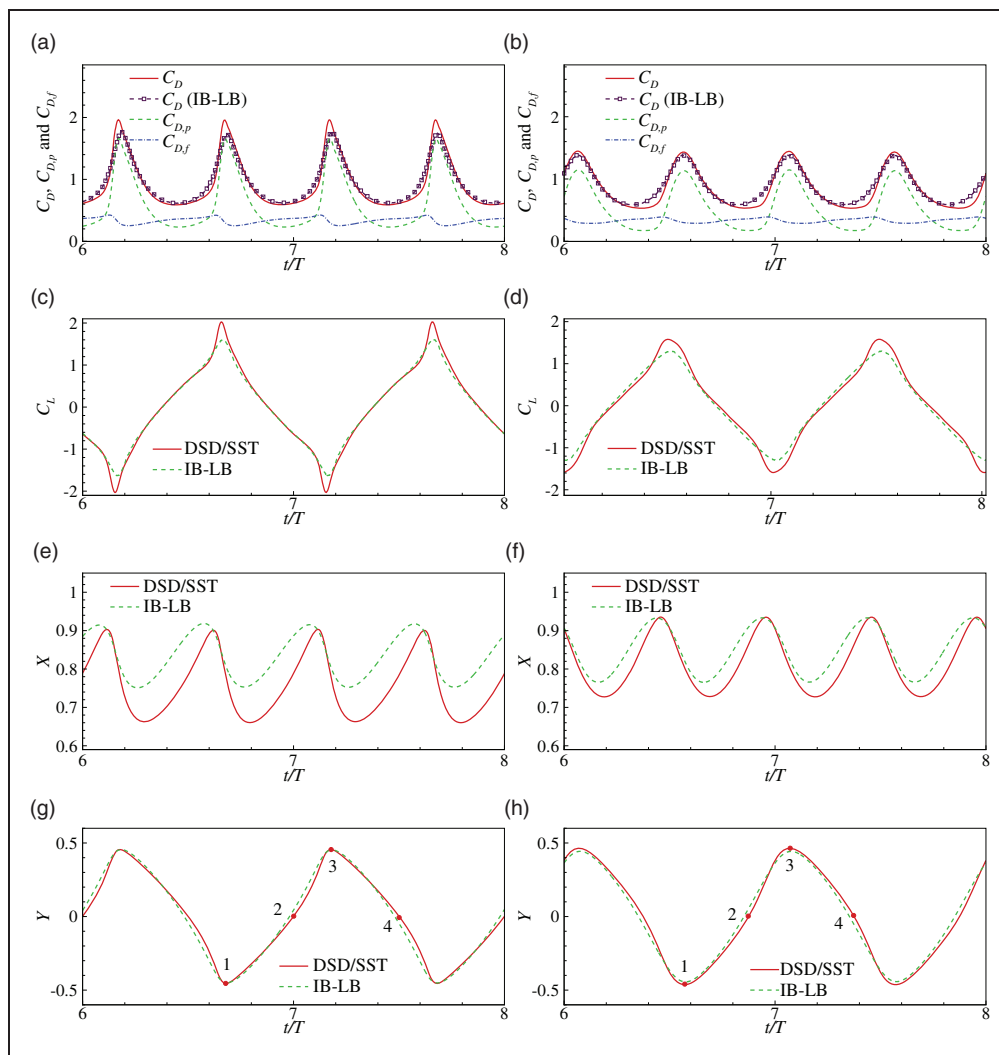

Figure 4. Drag and lift coefficients and the X- and Y-coordinates of the trailing point of a plate flapping in an axial flow. Left and right columns are, respectively, for $K_B = 10^{-4}$ and 10^{-3}.

look into the details, the discrepancies are obvious. First, the average drag coefficient calculated by the IB–LB method is larger than the value calculated by the DSD/SST method, while the lateral vibration amplitude and frequency are reverse. Second, the force peaks predicted by the IB–LB method is smaller compared to those predicted by the DSD/SST method, as demonstrated in Figure 4(a) to (d). Third, the vibration amplitude of the tail point in x-direction calculated by the IB–LB method is much smaller than that calculated by the DSD/SST method (see Figure 4(e) and (f)). Finally, the snapping event predicted by the DSD/SST method is more obvious than that predicted by the IB–LB method. These discrepancies are understandable, considering the major difference between these two methods: the DSD/SST employs body-fitted mesh and has higher accuracy near FSI interface; the IB–LB method is based the Cartesian mesh, and uses a smooth approximation of the Dirac's delta function to achieve a "diffuse-boundary" approach of the FSI interface.

Consequently, there is larger numerical diffusion in the IB–LB method. This diffusion effect can be reduced to some extent by introducing the sharp-interface IB method (see literature[13,87]).

An obvious change when K_B increases from 10^{-4} to 10^{-3} is that the snapping event is inhibited, as indicated by the force and displacement histories shown in
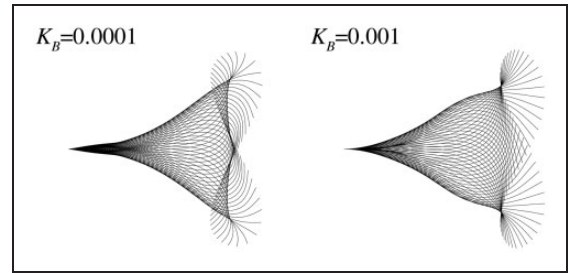

Figure 6. Deformation patterns of a flapping plate in an axial flow.
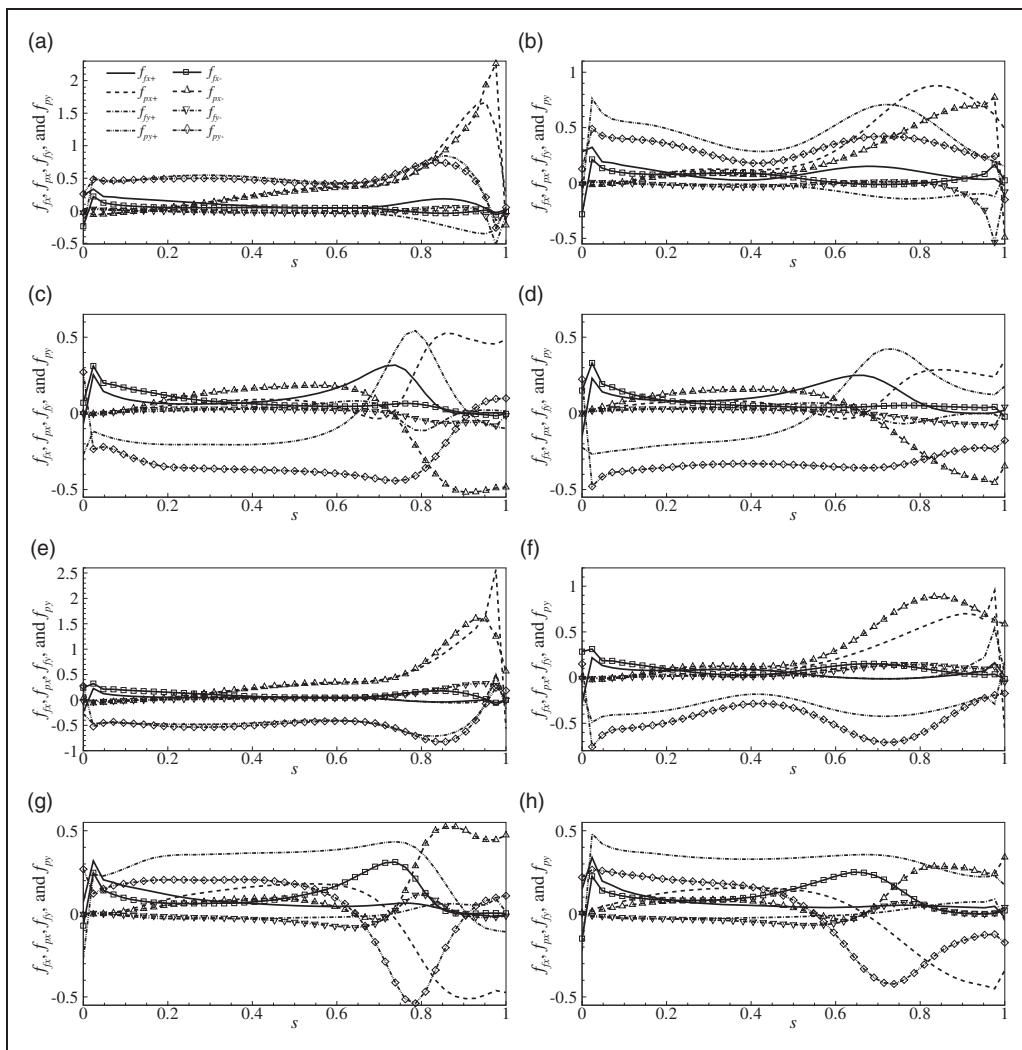

Figure 5. Local force coefficients on a flapping plate in an axial flow at four instants as indicated in Figure 4(g) and (h) during a flapping cycle. Left and right columns are, respectively, for $K_B = 10^{-4}$ and 10^{-3}.
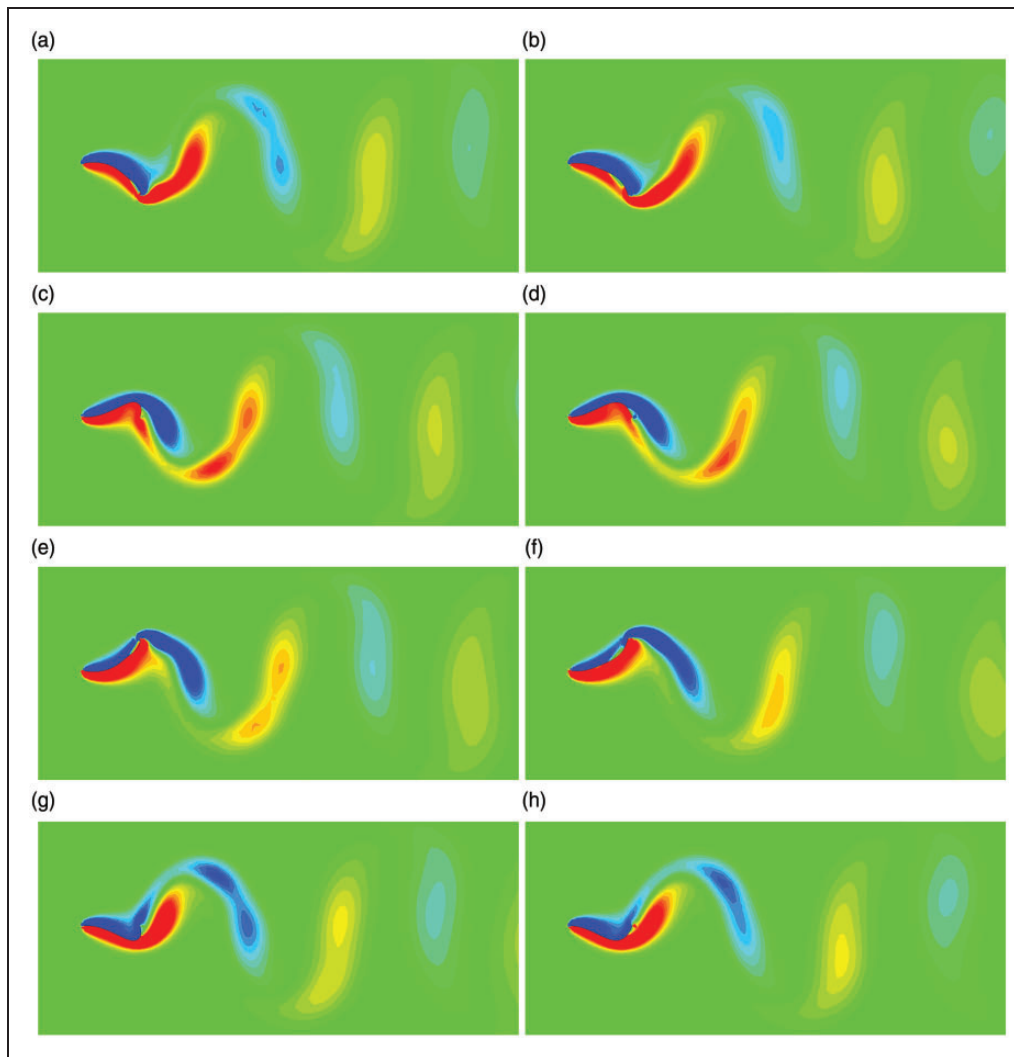
Figure 7. Vorticity fields at four instants as indicated in Figure 4(g) and (h) during a flapping cycle of the plate. Left and right columns are, respectively, for $K_B = 10^{-4}$ and 10^{-3}. The vorticity contours range from -4 (blue) to 4 (red).
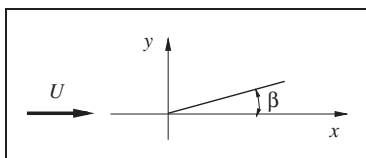

Figure 8. Schematic of a pitching flexible plate in a uniform flow.[29,30]

Figure 4 and the deformation patterns in Figure 6. This can be explained by the fact that the snapping motion is caused by the inertial effect of the flexible plate. When K_B increases, the inertial effect decreases. In addition, this snapping event causes the lift peaks. The smaller inertial effect produces smaller lift peaks, as shown in Figure 4(c) and (d). The strong snapping motion for $K_B = 10^{-4}$ leads to an interesting phenomenon: the vortices shedding from the trailing edge of the plate contain two cores, as shown in the left column of Figure 7. These two cores coalesce for $K_B = 10^{-3}$.

The last interesting observation is that the local viscous stress (see Figure 5) near $s = 0.75$ is larger at 2 and 4 instants (as marked in Figure 4(g) and (h)), compared to other regions and other instants. This is caused by the deflection extruding into the free stream which makes the shear layer thinner. It is also noted that this viscous stress is smaller for $K_B = 10^{-3}$, since the extrusion is smaller.

A pitching flexible plate

The second case is the flexible deformation of a pitching plate. The computational configuration is shown in Figure 8, where a flexible plate undergoes a prescribed pitching motion about its leading edge which is located at the origin. The pitching motion is described by $\beta = \beta_0 \sin(2\pi f t)$, where β_0 is the pitching amplitude and f denotes the pitching frequency. The computational domain and the mesh are the same as those used in the previous problem. The time step is $1/(500f)$ used in the DSD/SST solver and $0.001L/U$ (about $1/(1666f)$) is used in the IB–LB solver. Two
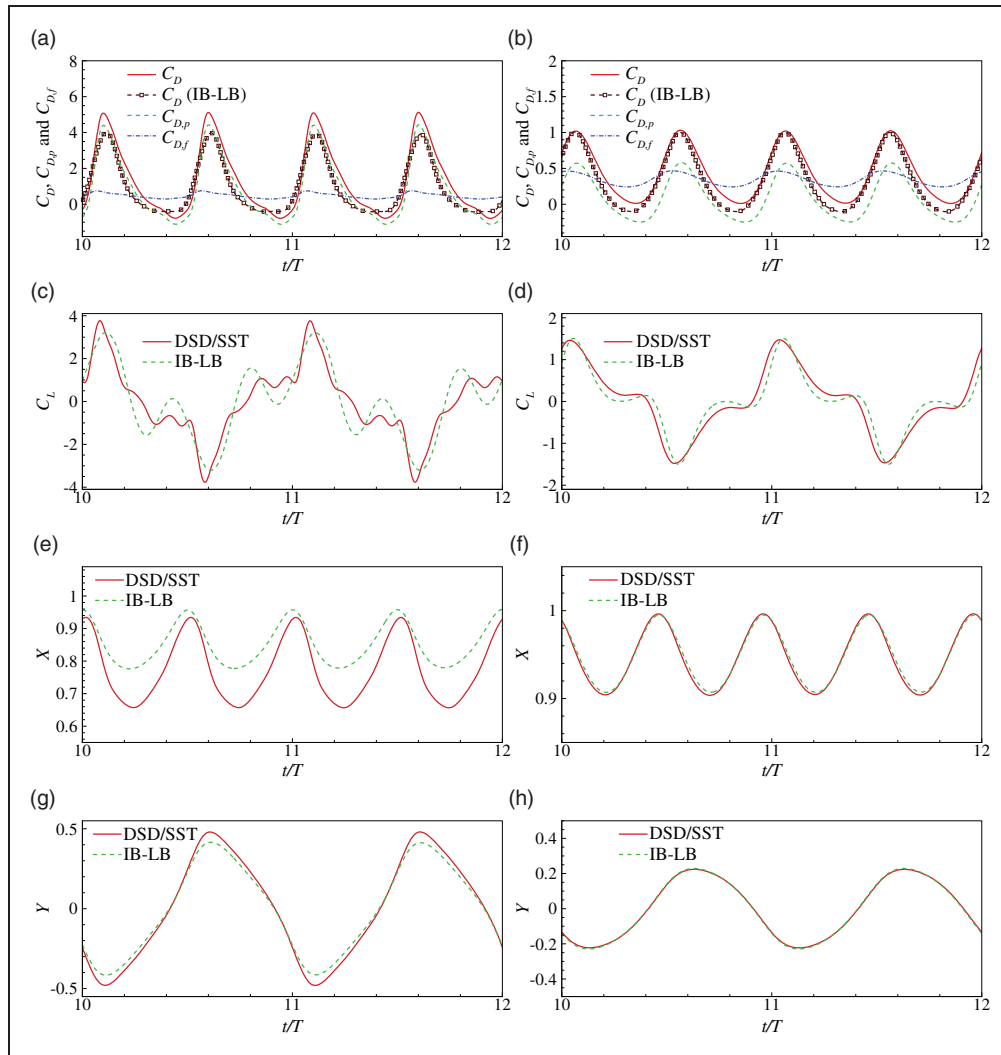
Figure 9. Drag and lift coefficients and *X*- and *Y*-coordinates of the trailing point of a pitching plate in a uniform flow. Left and right columns are, respectively, for $K_B = 0.0625$ and 0.125.

bending rigidities are considered: $K_B = 0.0625$ and 0.125. Other parameters are set as: $f^* = fL/U = 0.6$, $\beta_0 = 30°$, Re $= 100$, $S = 1$, and $K_S = 500$.

Simulations are conducted until the position of the trailing point of the pitching plate is periodic. Figures 9 to 12 show the force coefficients, tail position, deformation pattern of the plate, and vorticity fields.

Similar to the previous case, the results predicted by the DSD/SST method and the IB–LB method are consistent with each other and some discrepancies are observed. The overall trend for $K_B = 0.125$ is more consistent compared to that for $K_B = 0.0625$. The difference of the flapping amplitude is about 12% for $K_B = 0.0625$ and 3% for $K_B = 0.125$; and the difference of average drag is 28% for $K_B = 0.0625$ and 23% for $K_B = 0.125$. The drag coefficient for $K_B = 0.0625$ predicted by the DSD/SST solver is larger than that predicted by the IB-LB solver in $0.05T - 0.4T$ and

$0.55T - 0.9T$. This is caused by the larger deflection (especially the *X*-motion) in these regions. However, it is smaller than that predicted by the IB-LB solver in $0.4T - 0.55T$ and $0.9T - 1.05T$. This can be explained by two factors: smaller deflections and larger damping of the IB-LB method.

If we just look at the DSD/SST results, the average drag coefficient for $K_B = 0.0625$ is 1.321, which is almost three times as much as that for $K_B = 0.125$, whose average drag coefficient is 0.438. This is caused by the difference of the tail motion amplitude, as shown in Figures 9(g) and (h) and 11. Specifically, the lateral motion amplitude for $K_B = 0.0625$ is 0.961, while that for $K_B = 0.125$ is 0.448. It was shown in Ristroph and Zhang[88] that the plate of larger amplitude in a 2D uniform flow is likely to experience larger drag.

Similar to the flow-induced vibration of a highly flexible plate in an axial flow, here we also observe the snapping motion which causes the peaks of the
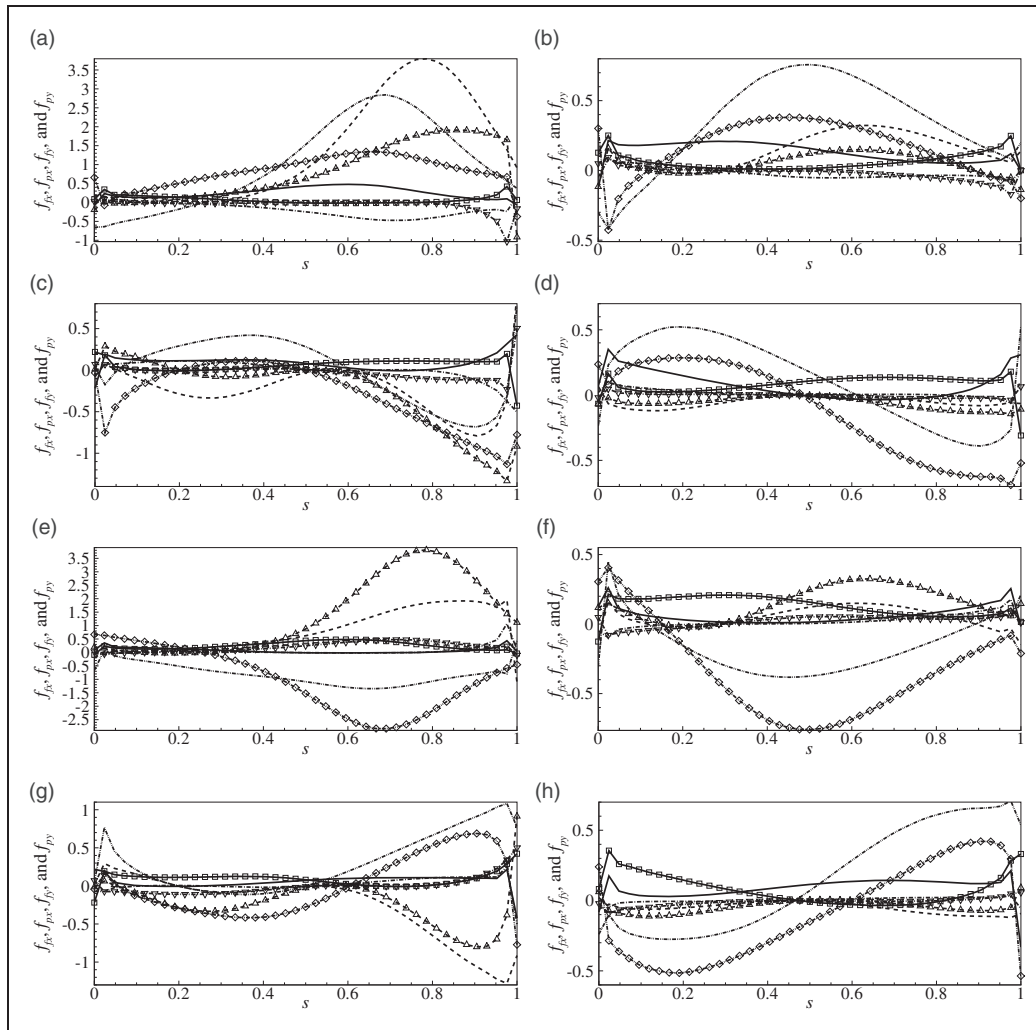
Figure 10. Local force coefficients on a pitching plate at four instants as indicated in Figure 9(g) and (h) during a flapping cycle. Left and right columns are, respectively, for $K_B = 0.0625$ and 0.125. The legend is the same as that in Figure 5.

lift coefficient. The larger lateral amplitude for $K_B = 0.0625$ leads to more obvious snapping event and larger lift peaks. An interesting observation is that the time history of the lift coefficient for $K_B = 0.0625$ experiences high frequency oscillations (see Figure 9(c)) whose frequency is about 10 times of the pitching frequency and is approximately the same as the nature frequency of the plate. Therefore, these oscillations might be caused by the natural vibration of the plate.

Another interesting observation is that the larger deformation for $K_B = 0.0625$ dramatically changes the vortex wake compared to the higher bending rigidity cases (see Figure 12), such as $K_B = 0.125$ in this paper and 0.25 and 0.5 in our previous papers.[29,30] Using the concepts in two cylinders in tandem arrangement,[73] the wake for $K_B = 0.125$ is a single bluff-body mode which contains a single von Kármán street wake (see right column in Figure 12), while the wake for $K_B = 0.0625$ is a secondary vortex formation mode, where the vortices with the same
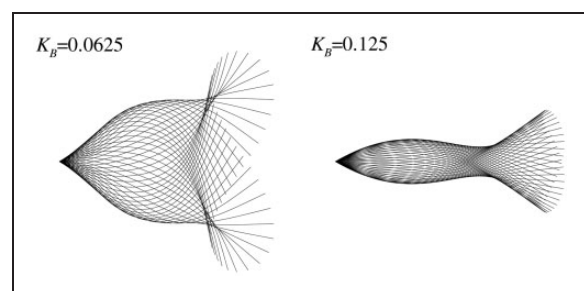

Figure 11. Deformation patterns of a pitching plate in a uniform flow.

sign are arranged in-line on each side of the wake (see left column in Figure 12). As the vortices convect downstream, the neighboring vortices in each row merge with each other and form a secondary vortex street with a lower frequency and a larger scale in the far downstream wake. Similar vortex merging process has been reported in multiple plates in side-by-side arrangement.[5]
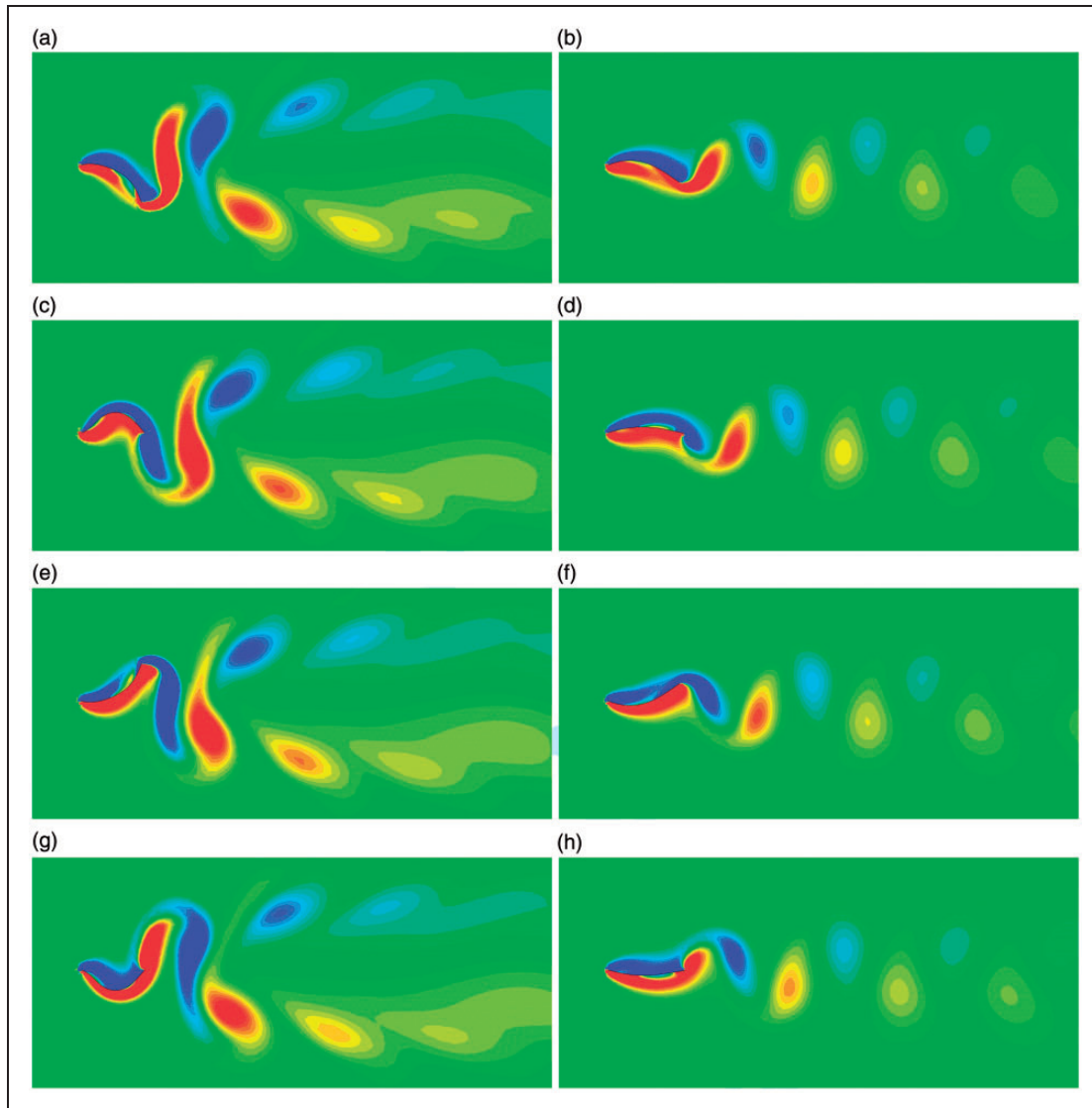
Figure 12. Vorticity fields at four instants as indicated in Figure 9(g) and (h) during a flapping cycle. Left and right columns are, respectively, for $K_B = 0.0625$ and 0.125. The vorticity contours range from -4 (blue) to 4 (red).

Conclusion

In this paper, the benchmark numerical solutions for two 2D FSI problems including the flow-induced vibration of a highly flexible plate in an axial flow and a pitching flexible plate have been presented. The solutions are obtained by using two partitioned FSI methods: one is based on the DSD/SST fluid solver and the FD structure solver, and the other is based on the LB method for the fluid dynamics, the same finite-difference method for the structural dynamics and IB method for FSI coupling. In the DSD/SST solver, the mesh moving strategy has been improved to prevent severe mesh distortion in cases where the boundary does not oscillate periodically or it needs a long time to establish a periodic motion. Results of the force coefficients, tail position, plate deformation pattern and vorticity fields have been presented and discussed for different values of the

bending coefficient, K_B. In addition, the results from the DSD/SST implementation have been compared with those from the IB-LB method. Finally, the differences caused by the bending rigidity have been discussed in terms of the forces, vibration amplitude and vorticity fields.

The results show that both the DSD/SST method and the IB–LB method are able to capture the major flow features. We also observe discrepancies between the two sets of results. Specifically, for flow-induced vibration of a highly flexible plate in an axial flow, the DSD/SST method predicts a lower average drag, higher lateral oscillation amplitude, higher frequency, higher/sharper force peaks, and more obvious snapping event compared to those predicted by the IB–LB method. For the pitching flexible plate, the discrepancy is much larger for $K_B = 0.0625$ compared to that for $K_B = 0.125$ which is associated with the flapping amplitude variations. These discrepancies are due to

the lower numerical diffusion of the DSD/SST method. For both problems studied, smaller K_B or higher inertial effect leads to more obvious snapping event and thus larger force peaks.

These observations (i.e. the same major flow features and the discrepancies of details) show that both the DSD/SST method and the IB–LB method are useful in studying FSI problems. If one is interested in the large scale flow features, FSI processes and/or engineering optimization, the IB–LB method, which is usually simple in mesh generation and efficient in solving flow field, is preferred; if one is interested in the small-scale flow details and the local force distributions, the DSD/SST method, which is complex in mesh treatment and computationally expensive, is a better choice.

The simulations presented in this work can be taken as benchmark cases for future validation purpose of newly developed FSI methods. To apply the data presented, a straightforward method is to compare the forces and/or flow fields predicted by a new method with those presented in this work. Based on the comparison, one is able to qualitatively evaluate the solver properties.

References

1. Zhu L and Peskin CS. Simulation of a flapping flexible filament in a flowing soap film by the immersed boundary method. *J Comput Phys* 2002; 179: 452–468.
2. Tezduyar TE, Sathe S, Keedy R, et al. Space–time finite element techniques for computation of fluid–structure interactions. *Comput Meth Appl Mech Eng* 2006; 195: 2002–2027.
3. Tezduyar TE, Sathe S and Stein K. Solution techniques for the fully-discretized equations in computation of fluid–structure interactions with the space–time formulations. *Comput Meth Appl Mech Eng* 2006; 195: 5743–5753.
4. Tian FB, Luo H, Zhu L, et al. An immersed boundary-lattice Boltzmann method for elastic boundaries with mass. *J Comput Phys* 2011; 230: 7266–7283.
5. Tian FB, Luo H, Zhu L, et al. Coupling modes of three filaments in side-by-side arrangement. *Phys Fluids* 2011; 23: 111903.
6. Tian FB, Lu XY and Luo H. Onset of instability of a flag in uniform flow. *Theor Appl Mech Lett* 2012; 2: 022005.
7. Tian FB. Role of mass on the stability of flag/flags in uniform flow. *Appl Phys Lett* 2013; 103: 034101.
8. Tian FB, Luo H, Song J, et al. Force production and asymmetric deformation of a flexible flapping wing in forward flight. *J Fluids Struct* 2013; 36: 149–161.
9. Wu J, Shu C, Zhao N, et al. Numerical study on the power extraction performance of a flapping foil with a flexible tail. *Phys Fluids* 2015; 27: 013602.
10. Wu J, Wu J, Tian FB, et al. How a flexible tail improve the power extraction efficiency of a semi-activated flapping foil system: a numerical study. *J Fluids Struct* 2015; 54: 886–899.
11. Tian FB, Chang S, Luo H, et al. Computational modeling of flow-induced vocal fold vibration. In: *Annual ORNL biomedical science and engineering conference (BSEC 2013)*, Oak Ridge, TN, 21–23 May 2013.
12. Tian FB, Chang S, Luo H, et al. A 3D numerical simulation of wave propagation on the vocal fold surface. In: *Proceedings of the 10th international conference on advances in quantitative laryngology, voice and speech research*. Cincinnati, OH, 3–4 June 2013, pp.94921483.
13. Tian FB, Dai H, Luo H, et al. Fluid–structure interaction involving large deformations: 3D simulations and applications to biological systems. *J Comput Phys* 2014; 258: 451–469.
14. Deng HB, Xu YQ, Chen DD, et al. On numerical modeling of animal swimming and flight. *Comput Mech* 2013; 52: 1221–1242.
15. Takizawa K, Bazilevs Y, Tezduyar TE, et al. ST and ALE-VMS methods for patient-specific cardiovascular fluid mechanics modeling. *Math Models Meth Appl Sci* 2014; 24: 2437–2486.
16. Takizawa K, Bazilevs Y, Tezduyar TE, et al. Engineering analysis and design with ALE-VMS and space–time methods. *Arch Comput Meth Eng* 2014; 21: 481–508.
17. Tezduyar TE. Stabilized finite element formulations for incompressible flow computations. *Adv Appl Mech* 1992; 28: 1–44.
18. Tezduyar TE, Behr M, Mittal S, et al. A new strategy for finite element computations involving moving boundaries and interfaces – the deforming-spatial-domain/space–time procedure: II. Computation of free-surface flows, two-liquid flows, and flows with drifting cylinders. *Comput Meth Appl Mech Eng* 1992; 94: 353–371.
19. Tezduyar TE, Behr M and Liou J. A new strategy for finite element computations involving moving boundaries and interfaces – the deforming-spatial-domain/space–time procedure: I. The concept and the preliminary numerical tests. *Comput Meth Appl Mech Eng* 1992; 94: 339–351.

20. Tezduyar TE. Computation of moving boundaries and interfaces and stabilization parameters. *Int J Numer Meth Fluids* 2003; 43: 555–575.

21. Tezduyar TE and Sathe S. Modeling of fluid–structure interactions with the space–time finite elements: solution techniques. *Int J Num Meth Fluids* 2007; 54: 855–900.

22. Takizawa K and Tezduyar TE. Multiscale space–time fluid–structure interaction techniques. *Comput Mech* 2011; 48: 247–267.

23. Takizawa K and Tezduyar TE. Space–time fluid–structure interaction methods. *Math Models Meth Appl Sci* 2012; 22: 1230001.

24. Mittal S and Tezduyar T. A finite element study of incompressible flows past oscillating cylinders and airfoils. *Int J Numer Meth Fluids* 1992; 15: 1073–1118.

25. Tezduyar TE. Interface-tracking and interface-capturing techniques for finite element computation of moving boundaries and interfaces. *Comput Meth Appl Mech Eng* 2006; 195: 2983–3000.

26. Tezduyar TE. Finite elements in fluids: stabilized formulations and moving boundaries and interfaces. *Comput Fluids* 2007; 36: 191–206.

27. Bazilevs Y, Takizawa K and Tezduyar TE. Challenges and directions in computational fluid–structure interaction. *Math Models Meth Appl Sci* 2013; 23: 215–221.

28. Tian FB, Bharti RP and Xu YQ. Deforming-Spatial-Domain/Stabilized Space-Time (DSD/SST) method in computation of non-Newtonian fluid flow and heat transfer with moving boundaries. *Comput Mech* 2014; 53: 257–271.

29. Tian FB. FSI modeling with the DSD/SST method for the fluid and finite difference method for the structure. *Comput Mech* 2014; 54: 581–589.

30. Tian FB, Wang Y, Young J, et al. An FSI solution technique based on the DSD/SST method and its applications. *Math Model Meth Appl Sci* 2015; 25: 2257–2285.

31. Brooks AN and Hughes TJR. Streamline upwind/Petrov–Galerkin formulations for convection dominated flows with particular emphasis on the incompressible Navier–Stokes equations. *Comput Methods Appl Mech Eng* 1982; 32: 199–259.

32. Hughes TJR and Tezduyar TE. Finite element methods for first-order hyperbolic systems with particular emphasis on the compressible Euler equations. *Comput Methods Appl Mech Engrg* 1984; 85: 217–284.

33. Tezduyar TE, Mittal S, Ray SE, et al. Incompressible flow computations with stabilized bilinear and linear equal-order-interpolation velocity-pressure elements. *Comput Meth Appl Mech Eng* 1992; 95: 221–242.

34. Mittal S and Tezduyar TE. Parallel finite element simulation of 3D incompressible flows–fluid-structure interactions. *Int J Numer Meth Fluids* 1995; 21: 933–953.

35. Johnson AA and Tezduyar TE. Advanced mesh generation and update methods for 3D flow simulations. *Comput Mech* 1999; 23: 130–143.

36. Tian FB, Lu XY and Luo H. Propulsive performance of a body with a traveling wave surface. *Phys Rev E* 2012; 86: 016304.

37. Takizawa K, Henicke B, Puntel A, et al. Space–time techniques for computational aerodynamics modeling of flapping wings of an actual locust. *Comput Mech* 2012; 50: 743–760.

38. Takizawa K, Kostov N, Puntel A, et al. Space–time computational analysis of bio-inspired flapping-wing aerodynamics of a micro aerial vehicle. *Comput Mech* 2012; 50: 761–778.

39. Takizawa K, Henicke B, Puntel A, et al. Computer modeling techniques for flapping-wing aerodynamics of a locust. *Comput Fluids* 2013; 85: 125–134.

40. Takizawa K, Henicke B, Puntel A, et al. Space–time computational techniques for the aerodynamics of flapping wings. *J Appl Mech* 2012; 79: 010903.

41. Tian FB, Xu YQ, Tang XY, et al. Study on a self-propelled fish swimming in viscous fluid by a finite element method. *J Mech Med Biol* 2013; 13: 1340012.

42. Takizawa K, Tezduyar TE and Kostov N. Sequentially-coupled space–time FSI analysis of bio-inspired flapping-wing aerodynamics of an MAV. *Comput Mech* 2014; 54: 213–233.

43. Takizawa K, Tezduyar TE and Buscher A. Space–time computational analysis of MAV flapping-wing aerodynamics with wing clapping. *Comput Mech* 2015; 55: 1131–1141.

44. Tian FB. A numerical study of linear and nonlinear kinematic models in fish swimming with the DSD/SST method. *Comput Mech* 2015; 55: 469–477.

45. Stewart WJ, Tian FB, Akanyeti O, et al. Refusing rainbow trout selectively exploit flows behind tandem cylinders. *J Exp Biol* 2016; 219: 2182–2191.

46. Tian FB, Young J and Lai JCS. A fem method for non-newtonian flow with moving boundaries and its application in fish swimming. In: *The 8th international conference on computational fluid dynamics*, Chengdu, China, 14–18 July 2014.

47. Peskin CS. Flow patterns around heart valves: a numerical method. *J Comput Phys* 1972; 10: 252–271.

48. Peskin CS. Numerical analysis of blood flow in the heart. *J Comput Phys* 1977; 25: 220–252.

49. Mittal R and Iaccarino G. Immersed boundary method. *Annu Rev Fluid Mech* 2005; 37: 239–261.

50. Griffith BE, Hornung RD, McQueen DM, et al. An adaptive, formally second order accurate version of the immersed boundary method. *J Comput Phys* 2007; 223: 10–49.

51. Ghias R, Mittal R and Dong H. A sharp interface immersed boundary method for compressible viscous flows. *J Comput Phy* 2007; 225: 528–553.

52. Wang W, Yin R, Hao D, et al. Modeling and simulation of fish-like swimming in a straight-line swimming state using immersed boundary method. *Adv Mech Eng* 2014; 2014: 489683.

53. Feng ZG and Michaelides EE. The immersed boundary-lattice Boltzmann method for solving fluid-particles interaction problems. *J Comput Phys* 2004; 195: 602–628.

54. Sui Y, Chew YT, Roy P, et al. A hybrid immersed-boundary and multi-block lattice Boltzmann method for simulating fluid and moving-boundaries interactions. *Int J Numer Meth Fluids* 2007; 53: 1727–1754.

55. Sui Y, Chew YT, Roy P, et al. A hybrid method to study flow-induced deformation of three-dimensional capsules. *J Comput Phys* 2008; 227: 6351–6371.

56. Xu YQ, Tian FB and Deng YL. An efficient red blood cell model in the frame of IB–LBM and its application. *Int J Biomath* 2013; 6: 1250061.

57. Wang Y and Elghobashi S. On locating the obstruction in the upper airway via numerical simulation. *Respir Physiol Neurobiol* 2014; 193: 1–10.

58. Kim Y and Peskin CS. Penalty immersed boundary method for an elastic boundary with mass. *Phys Fluids* 2007; 19: 053103.

59. Tian FB, Luo H, Zhu L, et al. Interaction between a flexible filament and a downstream rigid body. *Phys Rev E* 2010; 82: 026301.

60. Tian FB, Dai H, Luo H, et al. Computational fluid–structure interaction for biological and biomedical flows. In: *Proceedings of the ASME 2013 fluids engineering division summer meeting*, Incline Village, NV, 7–11 July 2013, pp.16408.

61. Tian FB, Young J and Lai JCS. Improving power-extraction efficiency of a flapping plate: From passive deformation to active control. *J Fluids Struct* 2014; 51: 384–392.

62. Landau LD and Lifshitz EM. *Theory of elasticity*. New York, NY: Pergamon, 1986.

63. Mittal S and Kumar V. Flow-induced oscillations of two cylinders in tandem and staggered arrangements. *J Fluids Struct* 2000; 15: 717–736.

64. Bellman R and Kalaba R. *Oquisilinearization and nonlinear boundary-value problems*. New York, NY: American Elsevier, 1965.

65. Ben-Isreal A. A Newton–Raphson method for the solution of systems of equations. *J Math Anal Appl* 1966; 15: 243–252.

66. Saad Y and Schultz MH. GMRES: a generalized minimal residual algorithm for solving nonsymmetric linear systems. *SIAM J Sci Stat Comput* 1986; 7: 856–869.

67. Saad Y. *Iterative methods for sparse linear systems*. 2nd ed. New York, NY: Society for Industrial and Applied Mathematics, 2003.

68. Connell BSH and Yue DKP. Flapping dynamics of a flag in a uniform stream. *J Fluid Mech* 2007; 581: 33–67.

69. Wu JZ, Pan ZL and Lu XY. Unsteady fluid-dynamic force solely in terms of control-surface integral. *Phys Fluids* 2005; 17: 098102.

70. Tian FB, Zhu L, Fok PW, et al. Simulation of a pulsatile non-Newtonian flow past a stenosed 2D artery with atherosclerosis. *Comput Biol Med* 2013; 43: 1098–1113.

71. Tezduyar T, Aliabadi S, Behr M, et al. Parallel finite element computation of 3D flows. *Computer* 1993; 26: 27–36.

72. Johnson AA and Tezduyar TE. Mesh update strategies in parallel finite element computations of flow problems with moving boundaries and interface. *Comput Meth Appl Mech Eng* 1994; 119: 73–94.

73. Wang SY, Tian FB, Jia LB, et al. The secondary vortex street in the wake of two tandem circular cylinders at low Reynolds number. *Phys Rev E* 2010; 81: 036305.

74. Chen S and Doolen GD. Lattice Boltzmann method for fluid flows. *Annu Rev Fluid Mech* 1998; 30: 329–364.

75. Guo ZL, Zheng CG and Shi BC. Discrete lattice effects on the forcing term in the lattice Boltzmann method. *Phys Rev E* 2002; 65: 046308.

76. Aidun CK and Clausen JR. Lattice-Boltzmann method for complex flows. *Annu Rev Fluid Mech* 2010; 42: 439–472.

77. Qian YH, D'Humières D and Lallemand P. Lattice BGK models for Navier–Stokes equation. *Europhys Lett* 1992; 17: 479–484.

78. Chai Z, Huang C, Shi B, et al. A comparative study on the lattice Boltzmann models for predicting effective diffusivity of porous media. *Intl J Heat Mass Transfer* 2016; 98: 687–696.

79. Xu YQ, Tian FB, Li HJ, et al. Red blood cell partitioning and blood flux redistribution in microvascular bifurcation. *Theor Appl Mech Lett* 2012; 2: 024001.

80. Xu YQ, Tang XY, Tian FB, et al. IB–LBM simulation of the haemocyte dynamics in a stenotic capillary. *Comput Method Biomec* 2014; 17: 978–985.

81. Tian FB. Deformation of a capsule in a power-law shear flow. *Computat Math Meth Med* 2016; 2016: 7981386.

82. Huang WX and Sung HJ. An immersed boundary method for fluid–flexible structure interaction. *Comput Meth Appl Mech Eng* 2009; 198: 2650–2661.

83. Zhang J, Liu NS and Lu XY. Locomotion of a passively flapping flat plate. *J Fluid Mech* 2010; 659: 43–68.

84. Hao J and Zhu L. A lattice Boltzmann based implicit immersed boundary method for fluid–structure interaction. *Comput Math Appl* 2010; 59: 185–193.

85. Zhu L, He G, Wang S, et al. An immersed boundary method by the lattice Boltzmann approach in three dimensions with application. *Comput Math Appl* 2011; 61: 3506–3518.

86. Ladd AJC. Numerical simulation of particulate suspensions via a discretized Boltzmann equation, part 1. theoretical foundation. *J Fluid Mech* 1994; 271: 285–309.

87. Mittal R, Dong H, Bozkurttas M, et al. A versatile sharp interface immersed boundary method for incompressible flows with complex boundaries. *J Comput Phys* 2008; 227: 4825–4852.

88. Ristroph L and Zhang J. Anomalous hydrodynamic drafting of interacting flapping flags. *Phys Rev Lett* 2008; 101: 194502.